Distilling the evolving contributions of anthropogenic aerosols and greenhouse gases to historical low-frequency surface ocean changes

Yue Dong[1,2], Jennifer E. Kay[1,3], Clara Deser[4], Antonietta Capotondi[1,5], Sara C. Sanchez[3]

[1]Cooperative Institute For Research in Environmental Sciences, University of Colorado Boulder, Boulder, CO
[2]Department of Atmospheric and Oceanic Sciences, University of California Los Angeles, Los Angeles, CA
[3]Department of Atmospheric and Oceanic Sciences, University of Colorado Boulder, Boulder, CO
[4]Climate and Global Dynamics Division, NCAR, Boulder, CO
[5]Physical Sciences Laboratory, NOAA, Boulder, CO

Key Points:

- Over the past century, GHG forced response is characterized by a single dominant mode while AER response consists of two distinct modes.
- AER's first mode features a monotonic increase in global AER and global cooling pattern opposite to the GHG warming pattern
- AER's second mode features the recent shift in AER emissions, which drives regional warming amplifying the GHG response

Corresponding author: Yue Dong, ydong@atmos.ucla.edu

Abstract

Anthropogenic aerosols (AER) and greenhouse gases (GHG) – the leading drivers of the forced historical change – produce different large-scale climate response patterns, with varying trend pattern correlations from negative to positive over the past century. To understand what caused the time-evolving comparison between GHG and AER responses, we apply a joint low-frequency component analysis on global sea-surface temperature and sea-surface salinity response over 1921-2020 from CESM1 single-forcing large ensemble simulations. While GHG response is well-described by its first leading mode, AER response consists of two distinct modes. The first one features global AER increase and global cooling, opposite to GHG-induced warming. The second mode features multidecadal variations in AER distributions, where the recent shift from North America/western Europe to southeast Asia emissions drives regional changes enhancing the GHG effect. We argue that AER can have both competing and synergistic effects with GHG, as their emissions change temporally and spatially.

Plain Language Summary

Anthropogenically forced climate change over the past century has been mainly caused by two types of emissions: greenhouse gases (GHG) and aerosols (AER). In general, sulfate aerosols from industrial sources can reflect shortwave radiation to yield a cooling effect opposite to the GHG warming effect. However, model simulations isolating GHG and AER forcings show that the large-scale climate effect of AER does not always dampen the GHG effect. Instead, over recent decades, AER have produced surface ocean response patterns more like the GHG response. Using a novel principle component analysis, we find that aerosols have driven two distinct modes of climate change patterns over the historical period. The first mode is associated with global aerosol increase, resulting in global-wide cooling damping the GHG-induced warming. The second mode is associated with the shift in aerosol emissions from north America/western Europe to southeast Asia, which drives regional changes enhancing the GHG effect. Our results highlight the importance of considering the temporal and spatial evolutions of AER emissions in assessing GHG and AER climate effects and attributing historical anthropogenic climate changes to GHG and AER forcings.

1 Introduction

Anthropogenically forced climate change over the past century has been primarily driven by two components: greenhouse gases (GHG) and anthropogenic aerosols (AER). These components modulate the global-mean surface temperature through distinct radiative effects (Myhre et al., 2014; Forster et al., 2021) - GHG cause surface warming due to absorption and re-emission of longwave radiation, while AER change energy budget through reflection or absorption of shortwave radiation by scattering (e.g., sulfate) or absorbing species (e.g., black carbon). Additionally, AER have indirect effects on climate through cloud-aerosol interactions, where aerosols can serve as cloud condensation nuclei affecting clouds' albedo, lifetime, and properties (Twomey, 1977; Ackerman et al., 2004). Over the past century, long-term increases in global-mean GHG and AER have led to a large cancellation between GHG-induced warming and AER-induced cooling effects (Deser et al., 2020).

While a clear opposing effect from GHG and AER on global-mean surface temperature has been found, comparing the spatial patterns of their climate responses has been less straightforward. Focusing on global GHG and AER forcings in the 20th century, Xie et al. (2013) found that the first leading modes of climate response patterns to GHG and AER bear a great resemblance, suggesting that large-scale climate responses are governed by the same ocean-atmosphere feedbacks intrinsic to the climate system. Wang et al. (2016) further examined the differences in those leading modes, highlighting the unique features of AER forced response associated with interhemispheric temperature asymmetry and cross-equatorial circulation change.

The spatial distributions of GHG and AER forcings add additional complexity to the comparison. Unlike well-mixed GHG, AER emissions have much richer structures in their spatial distributions and temporal evolution (Deser et al., 2020). Emissions from North America (NA) and western Europe (EU) have dominated the global total AER loading since the early decades of the 20th century until the 1970s, after which they have declined substantially following emission regulations. On the other hand, emissions from southeast Asia (SA) have been increasing gradually since the 1950s, and more recently, have surpassed the emissions from NA and EU since the 1990s. This transition of major AER sources has been found to cause large-scale climate changes in a different way than global-mean AER change (Kang et al., 2021; Wang & Wen, 2022), and to some extent can compensate for the global mean AER effect (Shi et al., 2022).

To isolate and quantify the respective contributions of GHG and AER to forced historical climate change, single-forcing large ensemble (SF-LE) simulations within fully-coupled global climate models (GCMs) have provided valuable insights. Using CESM1 SF-LE, Deser et al. (2020) found that the contributions of GHG and AER to the large-scale patterns of total forced trends vary over time, with AER being the dominant driver before the 1970s and GHG dominating thereafter. Wang and Wen (2022) further extended the analysis to CMIP5 multi-model comparisons, highlighting both similarities and disparities in the spatial patterns of the trends driven by AER and GHG.

To recap the literature and to illustrate the evolving contributions of GHG and AER to forced historical trends, we begin by showing the ensemble-mean response in CESM1 SF-LE for two 40-year periods, 1940-1980 and 1980-2020. Figure 1 shows the trend patterns for sea-surface temperature (SST) and sea-surface salinity (SSS), and key atmospheric variables coupled with them, sea level pressure (SLP) and surface water fluxes (i.e., precipitation minus evaporation, P-E). We compare these trend patterns forced by all forcings ("ALL"; from the CESM1 LE project, Kay et al. 2015), GHG, and AER (from Deser et al. 2020). As found in previous studies, during the early period (1940-1980; Fig. 1a), the total forced response is dominated by AER, featuring an inter-hemispheric contrast with pronounced cooling due to the SW absorption by AER and salinification trends in the northern hemisphere (NH) driven by an enhancement of Atlantic Meridional Overturning Circulation (AMOC; Menary et al., 2020) and increased sea-ice formation in the Arctic ocean. During recent decades (1980-2020; Fig. 1b), the total forced response has been dominated by GHG, featuring broad global warming, a "wet-get-wetter" precipitation pattern, and a "salty-get-saltier" SSS pattern, consistent with the literature (Held & Soden, 2006; Xie et al., 2010; Durack et al., 2012; Capotondi et al., 2012).

Perhaps more interestingly, the climate response patterns driven by GHG and AER largely oppose each other during the early period, but show some resemblance during the later period at regional scales (e.g., NH warming and Arctic freshening). We further compute the pattern correlations for running 40-yr trends in global SST and SSS between the ALL and single forcing (GHG or AER) ensemble-means, following Deser et al. (2020). As expected, the pattern correlations between ALL and GHG for both SST and SSS have increased steadily since the 1950s (red lines in Figs. 1c, d), suggesting the increasingly dominant role of GHG in modulating global climate. However, the pattern correlations between ALL and AER decreased only over the first half of the 20th century and have gradually rebounded over recent decades (blue lines in Figs. 1c, d). The same non-monotonic behavior is also found for the pattern correlation between GHG and AER (black lines in Figs. 1 c, d), indicating that the surface ocean response patterns to AER have become closer, not opposite, to those forced by GHG over recent decades.

This comparison between the evolving AER and GHG forced responses led us to ask: what caused the AER response to change over time, and particularly, to amplify

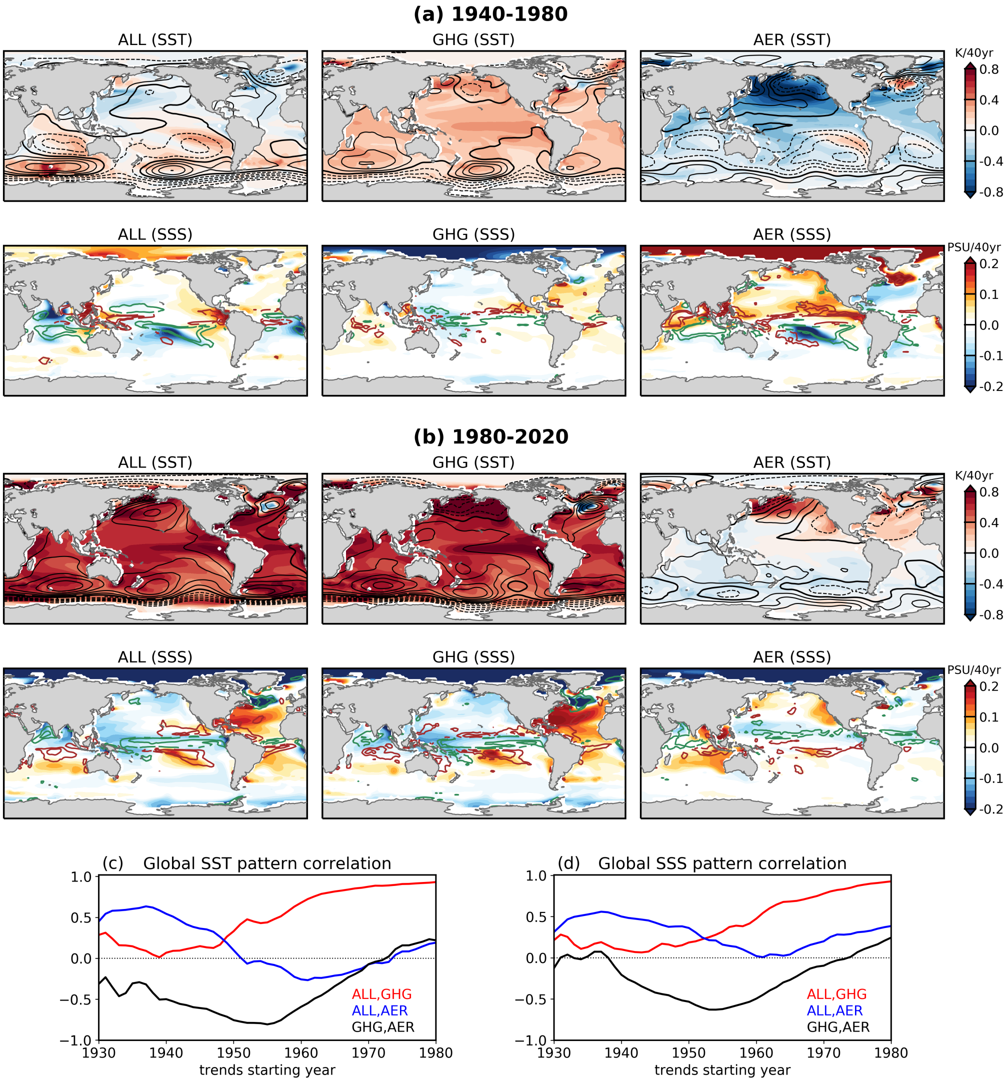

Figure 1. CESM1 ensemble-mean trend response to ALL, GHG and AER forcings, for (a) 1940-1980 and (b) 1980-2020. Black contours overlaid on the SST panels are SLP trends (contour interval is 0.16 hPa/40yr, zero contours are thickened, solid contours denote positive SLP trend, dashed contours denote negative SLP trend). Colored contours overlaid on the SSS panels are P-E trends (contour interval is 0.18 mm/day/40yr, zero contours are omitted; green denotes positive P-E and red denotes negative P-E). (c, d) Pattern correlations for 40-yr running trends in ensemble-mean (d) global SST and (e) global SSS between ALL, GHG and AER.

the GHG response over recent decades? Is it because of the decline of global AER emissions, or is it because of the change in the spatial distribution of those emissions, or both? And what implications does this have for detecting and attributing historical low-frequency surface ocean changes? Motivated by these questions, in this work we apply a principal component analysis to investigate the leading modes of low-frequency historical surface ocean changes driven by GHG and AER, and distill their evolving contributions to historical forced climate change.

2 Low-frequency component anlaysis

One of the caveats in the trend pattern analysis in Fig. 1 and other studies (e.g. Deser et al., 2020; Kang et al., 2021) is that these trends are computed over arbitrary time intervals, thus may not capture the whole series of the forced response and time-evolving forcing patterns. To achieve a more systematic assessment, other prior studies have utilized principal component (PC) analysis to linearly separate the total response into several empirical orthogonal functions (EOFs) (e.g., Xie et al., 2013; Wang et al., 2016; Bonfils et al., 2020). However, the EOF results can be affected by high-frequency natural variability (e.g., ENSO) that is not completely removed due to insufficient ensemble size. Therefore, to robustly examine the *low-frequency forced* response, we apply a low-frequency component analysis (LFCA; Wills et al. 2018) to the ensemble mean GHG and AER forced response from CESM1 SF-LE. In the following sections, we first introduce the LFCA method and the data analyzed (section. 2.1), and we next show the results of the leading low-frequency modes for the GHG and AER forced response (section 2.2).

2.1 The LFCA method and data

Unlike conventional PC analysis which maximizes total variance, LFCA finds a linear combination of EOFs that maximize the ratio of low-pass filtered variance to total variance, thereby isolating the leading modes of low-frequency variability (Wills et al., 2018). One can also apply LFCA to multiple spatial-temporal fields jointly, similar to the joint EOF analysis. Previous studies (Wills et al., 2022; Dörr et al., 2023; Bonan et al., 2023) suggest that the use of joint LFCA to account for low-frequency co-variability in multiple fields improves the isolation of long-term forced response.

Therefore, in this study we perform joint LFCA on global monthly SST and SSS anomalies over 1921 – 2020 to study low-frequency modes of forced historical surface ocean changes. The anomalies are relative to the 1921-2020 climatology. We take the SST and SSS response from the ensemble-mean of ALL, GHG and AER ensembles as part of CESM1 SF-LE (Deser et al. 2020), each containing 20 members. Note that original simulations in CESM1 SF-LE used the "all-but-one" forcing scenario – that is, all historical radiative forcing agents are prescribed except their GHG or AER is fixed at the 1920 conditions. The net effect of GHG and AER can be then obtained by subtracting these "all-but-one" SF simulations from the standard ALL simulations. We also note that in this set of LEs, AER specifically refers to industrial aerosols, not including biomass aerosols.

For the joint LFCA, we use a 15-year cut-off low-pass filter to isolate multidecadal low-frequency variability, and we retain the 10 leading EOFs, which in total account for 99.9%, 99% and 97% of the joint low-frequency variance for ALL, GHG and AER, respectively. Additionally, to understand the dynamical processes associated with each mode, we regress monthly SLP, precipitation (P), evaporation (E) and P-E anomalies onto the timeseries of each of the PCs.

Although we take the ensemble mean response first to remove random internal variability before performing the joint LFCA, one can also perform LFCA on each ensemble member to obtain (the best estimate of) its low-frequency forced response and then

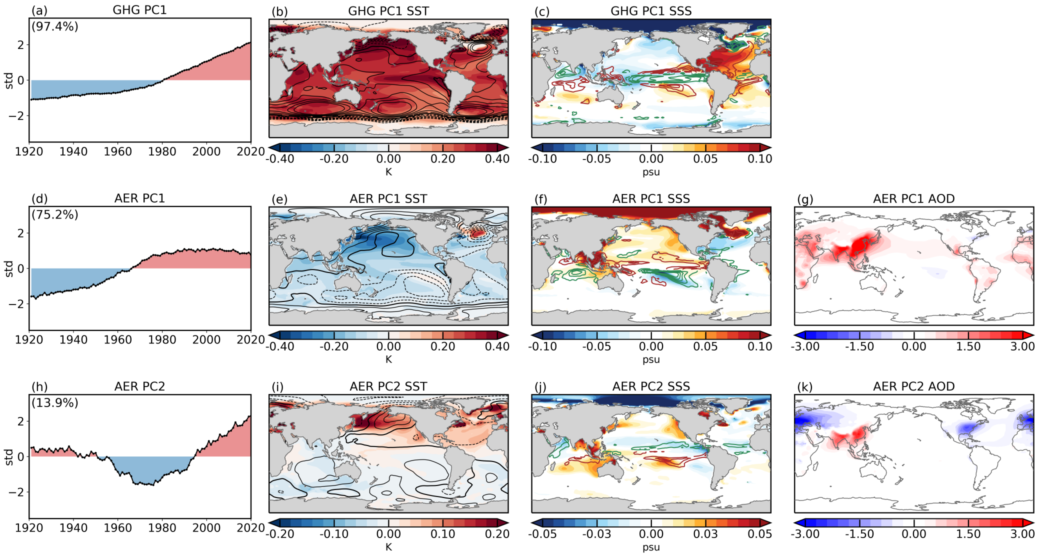

Figure 2. Leading low-frequency modes of GHG and AER ensemble-mean responses obtained from joint SST/SSS LFCA. Numbers in the corner of the timeseries plots show the low-frequency variance explained by the corresponding PC. SLP regressions are overlaid on the SST patterns (contour interval is 0.05 hPa, zero contours are thickened, solid contours denote positive SLP and dashed contours denote negative SLP); P-E regressions are overlaid on the SSS patterns (interval is 0.06 mm/day, zero contours are omitted, green denotes positive P-E and red denotes negative P-E). Regressions of aerosol optical depth at the 550nm (no unit, multiplied by 100) onto AER PC1 and PC2 are shown in panels (g) and (k).

average the leading modes across ensemble members (e.g., Wills et al., 2022; Kuo et al., 2023). We will show in the next section that the results remain the same regardless of which method is used (cf. Fig. 2 and Fig. S2)

2.2 Low-frequency modes of GHG and AER forced responses

Figure 2 shows the leading joint LFCA modes of SST and SSS for the GHG and AER forced responses. The GHG forced response is dominated by a single mode that explains 97.4% of the low-frequency variance; we will denote its timeseries as “GHG PC1” hereafter. The AER forced response consists of two leading modes, which both have strong multi-decadal variability and explain 75.2% and 13.9% of the total low-frequency variance, respectively. We will denote their timeseries as “AER PC1” and “AER PC2” hereafter.

The GHG PC1 has increased monotonically throughout the past century, with a pronounced positive trend starting from 1980 (Fig. 2a). The corresponding SST pattern is characterized by broad global warming and enhanced tropical eastern Pacific warming (i.e., the El Niño-like SST pattern), accompanied by a reduced tropical zonal SLP gradient (Fig. 2b). The global-scale warming causes precipitation to increase in the tropics and decrease in the broad subtropics (Fig. S1a), following the “wet-get-wetter” and “warmer get wetter” mechanism (Held & Soden, 2006; Xie et al., 2010). Associated with enhanced global-scale evaporation (Fig. S1b), the net P-E pattern links to a “salty-get-saltier” SSS pattern (Fig. 2c Durack et al., 2012; Sun et al., 2021), with an enhanced

SSS gradient between tropical and subtropical oceans as well as an amplified climatological contrast between the Pacific and Atlantic basins.

On the other hand, AER PC1 and PC2 feature distinct surface ocean patterns and time evolutions (Figs. 2d-k). By regressing aerosol optical depth (AOD) onto PC1 and PC2, we find that the first mode is associated with a globally increasing AOD pattern, with the largest source in east Asia (Fig. 2g). The positive AOD anomalies cause global-scale SST cooling by reflecting SW radiation, which is most pronounced in the north Pacific downstream of the east Asian AOD source (Fig. 2e). The AOD-induced surface cooling further reduces precipitation in east Asia extending to the north Pacific (Fig. S1c), along with the weakly decreased evaporation (Fig. S1d), leading to increased SSS in the north Pacific (Fig. 2f). Additionally, global cooling reduces runoff into the Arctic Ocean from sea ice melting, thereby increasing its SSS. Overall, AER PC1 increases through most of the 20th century, with the strongest positive trend from 1940 to 1980 and a negligible trend after 1980 (Fig. 2d).

By contrast, AER PC2 is associated with the relative difference in AOD between northeast America/western Europe and southeast Asia (Fig. 2k). This PC has a negative trend from the early 20th century to 1970 and a reversed (positive) trend from 1980 to present day (Fig. 2h), reflecting the transition of major AER emissions from NA/EU to SA over the course of the 20th century. In the positive phase of PC2, the negative AOD in NA/EU drives NH SST warming confined to mid-to-high latitudes (Fig. 2i) and Arctic freshening via increased runoff from sea-ice melting (Fig. 2j). The positive AOD in SA drives weak cooling (Fig. 2i) and drying locally in the Indo-Pacific ocean (Fig. S1e), which excites a Rossby wave response weakening the Aleutian Low (Fig. 2i; also see Smith et al. (2016); Dittus et al. (2021)). Due to the zonal-mean energy budget constraint, the ITCZ shifts northward towards the warmer NH as required by cross-equatorial heat transport (Kang et al., 2008; Hwang et al., 2013), resulting in enhanced precipitation north of the equator and reduced precipitation in the south (Fig. S1e). This zonal-mean precipitation dipole pattern further links to a meridional SSS gradient in the tropical Pacific, with decreased (increased) SSS in the north (south) (Fig. 2j).

In summary, the leading low-frequency modes of GHG and AER forced responses are diverse in both their spatial patterns and temporal evolutions. The GHG response can be largely captured by a single leading mode, which has increased monotonically throughout the past century. The AER forced response, however, features two distinct modes. AER PC1 is associated with increasing global AER emissions and resulting global cooling as well as enhanced regional responses in the NH western Pacific associated with east Asian emissions. AER PC2 represents a multidecadal variation in AER distribution, highlighting the emission shift from high-latitude NA/EU to low-latitude SA over recent decades. This mode features an inter-hemispheric SST gradient and a shift in zonal-mean precipitation and SSS anomalies. The spatial patterns of the two AER modes are consistent with previous studies; however, their relative order and temporal characteristics may depend on the period analyzed. For example, when accounting for a longer period including the 21st century, Gu et al. (2024) find that the AER shift mode (our 2nd mode) is the leading PC, followed by the AER global mode (our 1st mode).

3 Time-evolving contributions of the leading modes of AER and GHG responses

Having quantified the leading modes of AER and GHG responses, in this section, we aim to attribute the changes in the total forced response to these individual modes to gain physical insights.

First, we approximate the time-varying forced responses using their leading LFCA modes, and perform the pattern correlation analysis for running 40-yr trends in global

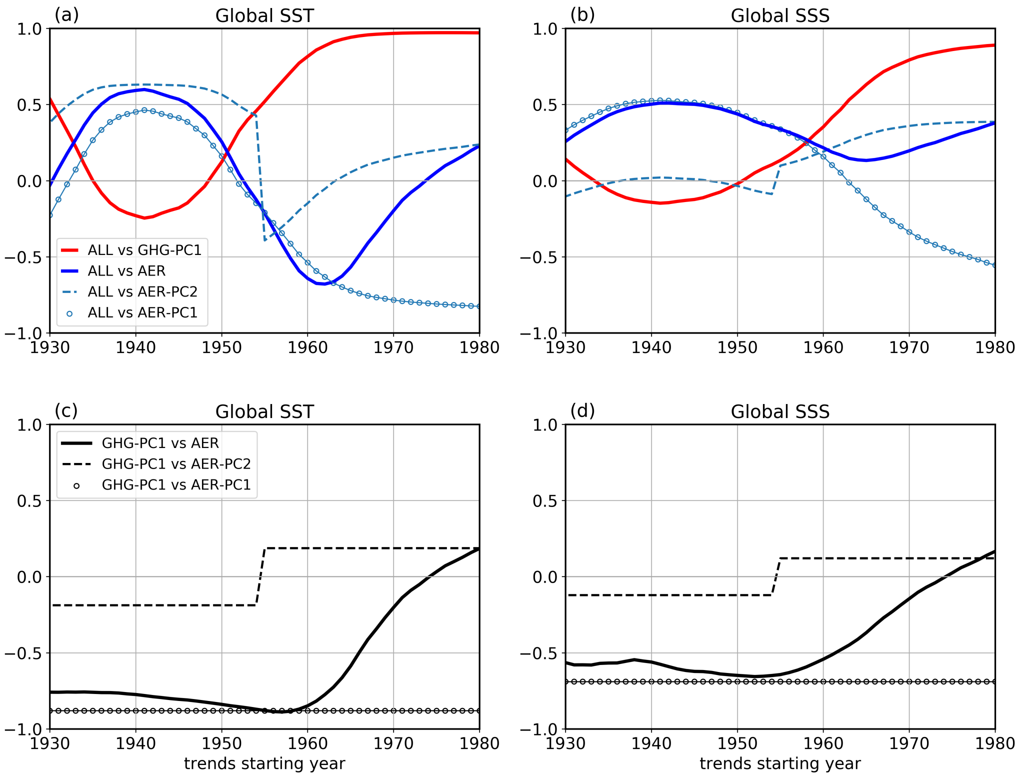

Figure 3. Pattern correlations for running 40-yr trends in (left) global SST and global SSS (right) response reconstructed using the LFCA leading modes, between (a, b) ALL and GHG or AER responses and (c, d) between GHG and AER responses.

SST and SSS as in Fig. 1 but use the PC-reconstructed responses. We find that using the first leading mode for GHG response and the leading two modes for AER and ALL response can faithfully reproduce the results of the simulated total response (cf. Fig. 3 and Fig. 1 c, d). The PC-based pattern correlations capture the increasingly high values between ALL and GHG and the non-monotonic evolution of the correlations between ALL and AER and between GHG and AER for both SST and SSS trend patterns.

Having verified that the LFCA modes can sufficiently reproduce the total response, now we come back to the questions raised at the beginning: what caused the AER response to change over time and to amplify (rather than offset) the GHG response over recent decades? More specifically, is it because of the change in AER PC1 associated with global AER emissions or the change in PC2 associated with shifting AER emissions, or both?

To answer these questions, we repeat the pattern correlation analysis with individual AER PCs. When only accounting for AER PC1, the pattern correlations between ALL and AER decrease monotonically after the 1940s (Figs 3a and b, blue circled lines), unlike the total AER response which bounces back after the 1960s (blue solid lines). Furthermore, the pattern correlations between AER PC1 and GHG PC1 stay at a constant negative value of -0.88 for SST and -0.69 for SSS (Figs. 3c and d, black circled lines), indicating that the response patterns associated with AER PC1 have continuously opposed those driven by GHG PC1. The high (albeit negative) pattern correlations between GHG PC1 and AER PC1 can already be seen in Fig. 2: both modes feature a global-wide SST response driven by global forcing (with sign reversed), and a similar hydrological cycle response constrained by global warming or cooling, all consistent with earlier findings by Xie et al. (2013).

Turning to AER PC2, although this mode has a much weaker pattern correlation with GHG PC1 overall, the correlation switches sign from negative to positive around mid-century (Figs. 3c and d, black dashed lines), suggesting that it is AER PC2, not PC1, that makes the total AER forced response patterns more similar to the GHG response patterns (Figs. 3c and d, black solid lines). The abrupt change in the running trend pattern correlations arises from the phase transition in the AER PC2 timeseries around the 1980s associated with the shift in major AER emissions from NA/EU to SA. As AER emissions increase over SA and decrease over NA/EU after the 1980s, this mode produce north Pacific warming, Arctic freshening and SH subtropical drying, similar to the GHG-induced local changes (Fig. 2), thus making the AER forced response more like the GHG response.

To further illustrate the different contributions of AER PC1 and PC2 to the total forced response, we show the trend patterns for AER and GHG PCs over 1940-1980 and 1980-2020 (Fig. 4). First, the PC-based trend patterns (Fig. 4, left two columns) are remarkably consistent with the actual simulated trend patterns (Fig. 1), confirming that using the leading modes can reproduce the total forced response. Next, turning to the trend patterns for AER PC1 and PC2 individually, we find that AER forced trends over 1940-1980 arise primarily from PC1 (Fig. 4a) and over 1980-2020 arise nearly entirely from PC2 (Fig. 4b). Moreover, the increase in global AOD from the early 20th century to the 1980s is predominately associated with PC1 and the moderate decline in global AOD afterward is caused mainly by PC2 (Fig. S3).

Overall, these findings suggest that both PC1 and PC2 make significant contributions to the AER response, but their roles vary in time. Over the first half of the 20th century until the 1980s, PC1 dominates the total AER forcing and the forced response, with patterns largely *opposite* to those of GHG. If the spatial pattern of AER emissions had remained unchanged from that of PC1 but continued to increase in magnitude over the past 40 years, the GHG response would have been largely compensated for by AER, resulting in a less detectable anthropogenically forced signal over the past century. How-

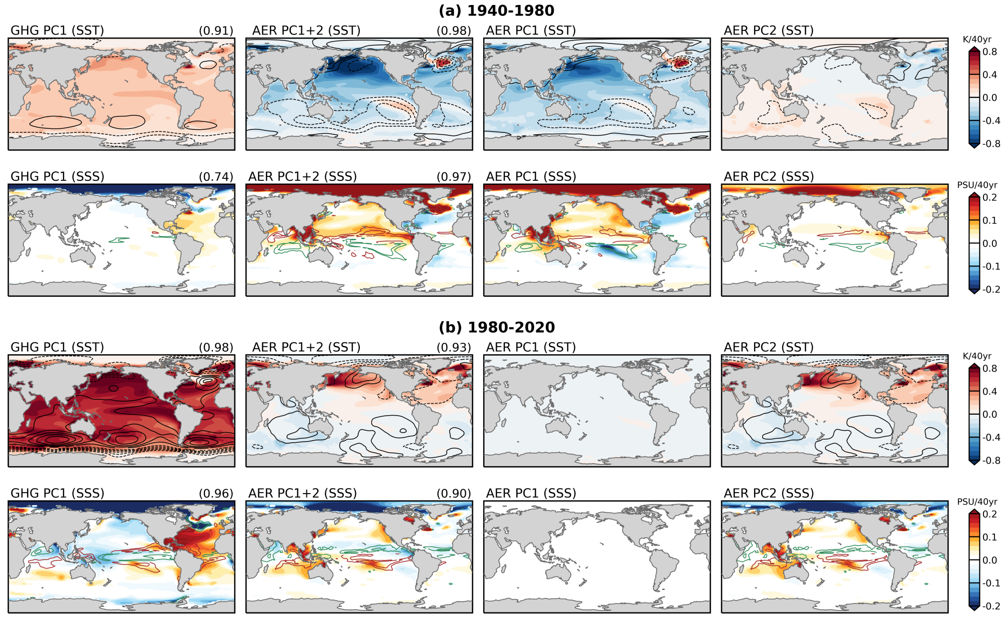

Figure 4. Similar to Fig. 1, except for the linear trend patterns associated with GHG and AER PCs for (a) 1940-1980, and (b) 1980-2020.

ever, the geographical distribution of AER emissions did change, shifting from NA/EU to SA, which led to the prominent phase transition in PC2 over recent decades. Although PC2 is associated with small global-mean AOD anomalies, the dynamical response associated with this AER shift mode can be large at regional scales. Some of the regional responses appear to *enhance* the GHG-induced changes, leading to a synergistic effect of AER with GHG over recent decades rather than a competing effect as in earlier periods.

4 Implications for detection and attribution

The time-evolving similarities and disparities between GHG and AER forced responses have important implications for detecting and attributing (D&A) historical climate change. Previous D&A studies, e.g. Bonfils et al. (2020), used an EOF approach with historical simulations and identified two externally forced fingerprints. They argued that the first one, featuring global warming and intensified wet-dry patterns, is driven by GHG, and that the second one, featuring an inter-hemispheric temperature contrast and meridional shift in ITCZ location, is driven by AER.

Using the SST/SSS joint LFCA, we also find two leading modes in the CESM1 ALL ensemble-mean response (Fig. S4), similar to the results of Bonfils et al. (2020). Indeed, at first glance, ALL PC1 and PC2 seem to bear a strong resemblance to GHG PC1 and AER PC1, respectively (Fig. 2). However, there are substantial differences between the patterns of ALL PC1 and GHG PC1. For example, GHG PC1 is characterized by a strong El Niño-like SST warming pattern (Fig. 2b), a zonal-mean wet-dry hydrological pattern (Fig. S1a) and a corresponding zonal SSS pattern (Fig. 2c). By contrast, ALL PC1 has a more uniform tropical SST pattern (Fig. S4b), a zonally-asymmetric precipitation pattern with drying in the west Pacific and wetting in the central Pacific (Fig. S5a), and a resulting SSS dipole pattern with increased salinity in the western Pacific (Fig. S4e). These mismatches, however, appear to be consistent with AER PC1, with a high pattern correlation of -0.7 for global SST between ALL PC1 (Fig. S4b) and AER PC1 (Fig. 2e). Similarly, while the response patterns of ALL PC2 are overall anti-correlated with AER PC1, there are noticeable spatial features that cannot be explained by AER PCs but rather resemble GHG PC1. Collectively, this suggests that the two modes of historical anthropogenic fingerprints obtained from CESM1 ALL simulations are forced by the combined effects of GHG and AER, rather than by each forcing agent individually as previously proposed (Bonfils et al., 2020).

Thus, we argue that previous D&A approaches that separate the leading modes of historical fingerprints to GHG and AER may be biased, as they don't account for the two distinct modes of AER response and their evolving synergistic and competing climate effects with GHG. Our CESM1 results suggest that robustly detecting and attributing historical forced climate change requires careful separation of GHG and AER responses, which are not mutually independent.

5 Summary

In this study, we have analyzed the leading modes of low-frequency climate responses to GHG and AER forcing and distilled their respective contributions to historical forced climate change in CESM1. While the GHG response can be well represented by a single dominant mode, the AER response features two distinct modes. The first mode is associated with an increase in global AER emissions over the past century, driving global-wide cooling and regional "wet-get-wetter" precipitation and "salty-get-saltier" salinity response patterns. This AER mode is spatially anti-correlated with the leading GHG mode, largely offsetting impacts from GHG, with some notable regional exceptions such as the western Pacific close to the source of east Asian AER emissions. The second AER mode is associated with a spatial redistribution of AER, featuring the shift of major emissions from north America/western Europe to southeast Asia over recent decades. This zonally asymmetric AER forcing pattern, however, yields meridional shifts in the zonal mean response of SST, hydrological and SSS, owing to large-scale energy budget constraints. Although this mode has a weaker correlation with the GHG response, the transition of this mode from a negative to positive phase over recent decades results in regional anomalies that can enhance the GHG-induced changes.

While our analysis has focused on the past century, the results and conclusions may change for future forcing scenarios. As global AER emissions are projected to decrease with clean-air efforts, AER PC1 will likely change sign in the future. Given the anti-correlation between AER PC1 and GHG PC1, the future AER effect may exacerbate GHG-induced climate change and enhance the detectability. Hence, it remains to be further investigated how our proposed framework will evolve in the future, accounting for various uncertainties arising from model structures, emission scenarios, and representations of AER (direct and indirect) forcings.

Open Research

The CESM1 Large Ensemble data (Kay et al., 2015) and single-forcing large ensemble data (Deser et al., 2020) are available from `https://www.cesm.ucar.edu/community-projects/lens` and `https://www.cesm.ucar.edu/working-groups/climate/simulations/cesm1-single-forcing-le`. Code to perform LFCA (Wills et al., 2018) is available on Github `https://github.com/rcjwills/lfca`.

Acknowledgments
YD, JEK and SCS are supported by NASA Oceanography Grant 80NSSC23K0358. The National Center for Atmospheric Research (NCAR) is sponsored by the National Sci-

ence Foundation under Cooperative Agreement 1852977. A.C. was supported by the NOAA Climate Program Office's CVP Program, and DOE Award # DE-SC0023228.

References

Ackerman, A. S., Kirkpatrick, M. P., Stevens, D. E., & Toon, O. B. (2004). The impact of humidity above stratiform clouds on indirect aerosol climate forcing. *Nature*, *432*(7020), 1014–1017.

Bonan, D. B., Dörr, J., Wills, R. C., Thompson, A. F., & Årthun, M. (2023). Sources of low-frequency variability in observed antarctic sea ice. *EGUsphere*, *2023*, 1–28.

Bonfils, C. J., Santer, B. D., Fyfe, J. C., Marvel, K., Phillips, T. J., & Zimmerman, S. R. (2020). Human influence on joint changes in temperature, rainfall and continental aridity. *Nature Climate Change*, *10*(8), 726–731.

Capotondi, A., Alexander, M. A., Bond, N. A., Curchitser, E. N., & Scott, J. D. (2012). Enhanced upper ocean stratification with climate change in the CMIP3 models. *Journal of Geophysical Research: Oceans*, *117*(C4).

Deser, C., Phillips, A. S., Simpson, I. R., Rosenbloom, N., Coleman, D., Lehner, F., ... Stevenson, S. (2020). Isolating the evolving contributions of anthropogenic aerosols and greenhouse gases: A new CESM1 large ensemble community resource. *Journal of climate*, *33*(18), 7835–7858.

Dittus, A. J., Hawkins, E., Robson, J. I., Smith, D. M., & Wilcox, L. J. (2021). Drivers of recent North Pacific decadal variability: The role of aerosol forcing. *Earth's Future*, *9*(12), e2021EF002249.

Dörr, J. S., Bonan, D. B., Årthun, M., Svendsen, L., & Wills, R. C. (2023). Forced and internal components of observed Arctic sea-ice changes. *The Cryosphere Discussions*, *2023*, 1–27.

Durack, P. J., Wijffels, S. E., & Matear, R. J. (2012). Ocean salinities reveal strong global water cycle intensification during 1950 to 2000. *science*, *336*(6080), 455–458.

Forster, P., Storelvmo, T., Armour, K., Collins, W., Dufresne, J.-L., Frame, D., ... others (2021). The earth's energy budget, climate feedbacks, and climate sensitivity.

Gu, P., Gan, B., Cai, W., Wang, H., & Wu, L. (2024). Future slower reduction of anthropogenic aerosols enhances extratropical ocean surface warming trends. *Geophysical Research Letters*, *51*(8), e2023GL107772.

Held, I. M., & Soden, B. J. (2006). Robust responses of the hydrological cycle to global warming. *Journal of climate*, *19*(21), 5686–5699.

Hwang, Y.-T., Frierson, D. M., & Kang, S. M. (2013). Anthropogenic sulfate aerosol and the southward shift of tropical precipitation in the late 20th century. *Geophysical Research Letters*, *40*(11), 2845–2850.

Kang, S. M., Held, I. M., Frierson, D. M., & Zhao, M. (2008). The response of the ITCZ to extratropical thermal forcing: Idealized slab-ocean experiments with a GCM. *Journal of Climate*, *21*(14), 3521–3532.

Kang, S. M., Xie, S.-P., Deser, C., & Xiang, B. (2021). Zonal mean and shift modes of historical climate response to evolving aerosol distribution. *Science Bulletin*, *66*(23), 2405–2411.

Kay, J. E., Deser, C., Phillips, A., Mai, A., Hannay, C., Strand, G., ... others (2015). The community earth system model (CESM) large ensemble project: A community resource for studying climate change in the presence of internal climate variability. *Bulletin of the American Meteorological Society*, *96*(8), 1333–1349.

Kuo, Y.-N., Kim, H., & Lehner, F. (2023). Anthropogenic aerosols contribute to the recent decline in precipitation over the US Southwest. *Geophysical Research Letters*, *50*(23), e2023GL105389.

Menary, M. B., Robson, J., Allan, R. P., Booth, B. B., Cassou, C., Gastineau, G., … others (2020). Aerosol-forced AMOC changes in cmip6 historical simulations. *Geophysical Research Letters*, *47*(14), e2020GL088166.

Myhre, G., Shindell, D., Bréon, F.-M., Collins, W., Fuglestvedt, J., Huang, J., … others (2014). Anthropogenic and natural radiative forcing. *Climate Change 2013-The Physical Science Basis*, 659–740.

Shi, J.-R., Kwon, Y.-O., & Wijffels, S. E. (2022). Two distinct modes of climate responses to the anthropogenic aerosol forcing changes. *Journal of Climate*, *35*(11), 3445–3457.

Smith, D. M., Booth, B. B., Dunstone, N. J., Eade, R., Hermanson, L., Jones, G. S., … Thompson, V. (2016). Role of volcanic and anthropogenic aerosols in the recent global surface warming slowdown. *Nature Climate Change*, *6*(10), 936–940.

Sun, Q., Du, Y., Xie, S.-P., Zhang, Y., Wang, M., & Kosaka, Y. (2021). Sea surface salinity change since 1950: Internal variability versus anthropogenic forcing. *Journal of Climate*, *34*(4), 1305–1319.

Twomey, S. (1977). Atmospheric aerosols.

Wang, H., & Wen, Y.-J. (2022). Climate response to the spatial and temporal evolutions of anthropogenic aerosol forcing. *Climate Dynamics*, *59*(5), 1579–1595.

Wang, H., Xie, S.-P., & Liu, Q. (2016). Comparison of climate response to anthropogenic aerosol versus greenhouse gas forcing: Distinct patterns. *Journal of Climate*, *29*(14), 5175–5188.

Wills, R. C., Dong, Y., Proistosecu, C., Armour, K. C., & Battisti, D. S. (2022). Systematic climate model biases in the large-scale patterns of recent sea-surface temperature and sea-level pressure change. *Geophysical Research Letters*, *49*(17), e2022GL100011.

Wills, R. C., Schneider, T., Wallace, J. M., Battisti, D. S., & Hartmann, D. L. (2018). Disentangling global warming, multidecadal variability, and El niño in Pacific temperatures. *Geophysical Research Letters*, *45*(5), 2487–2496.

Xie, S.-P., Deser, C., Vecchi, G. A., Ma, J., Teng, H., & Wittenberg, A. T. (2010). Global warming pattern formation: Sea surface temperature and rainfall. *Journal of Climate*, *23*(4), 966–986.

Xie, S.-P., Lu, B., & Xiang, B. (2013). Similar spatial patterns of climate responses to aerosol and greenhouse gas changes. *Nature Geoscience*, *6*(10), 828–832.

Supporting Information for "Distilling the evolving contributions of anthropogenic aerosols and greenhouse gases to historical low-frequency surface ocean changes"

Yue Dong[1,2], Jennifer E. Kay[1,3], Clara Deser[4], Antonietta Capotondi[1,5], Sara C. Sanchez[3]

[1]Cooperative Institute For Research in Environmental Sciences, University of Colorado Boulder, Boulder, CO

[2]Department of Atmospheric and Oceanic Sciences, University of California Los Angeles, Los Angeles, CA

[3]Department of Atmospheric and Oceanic Sciences, University of Colorado Boulder, Boulder, CO

[4]Climate and Global Dynamics Division, NCAR, Boulder, CO

[5]Physical Sciences Laboratory, NOAA, Boulder, CO

Contents of this file

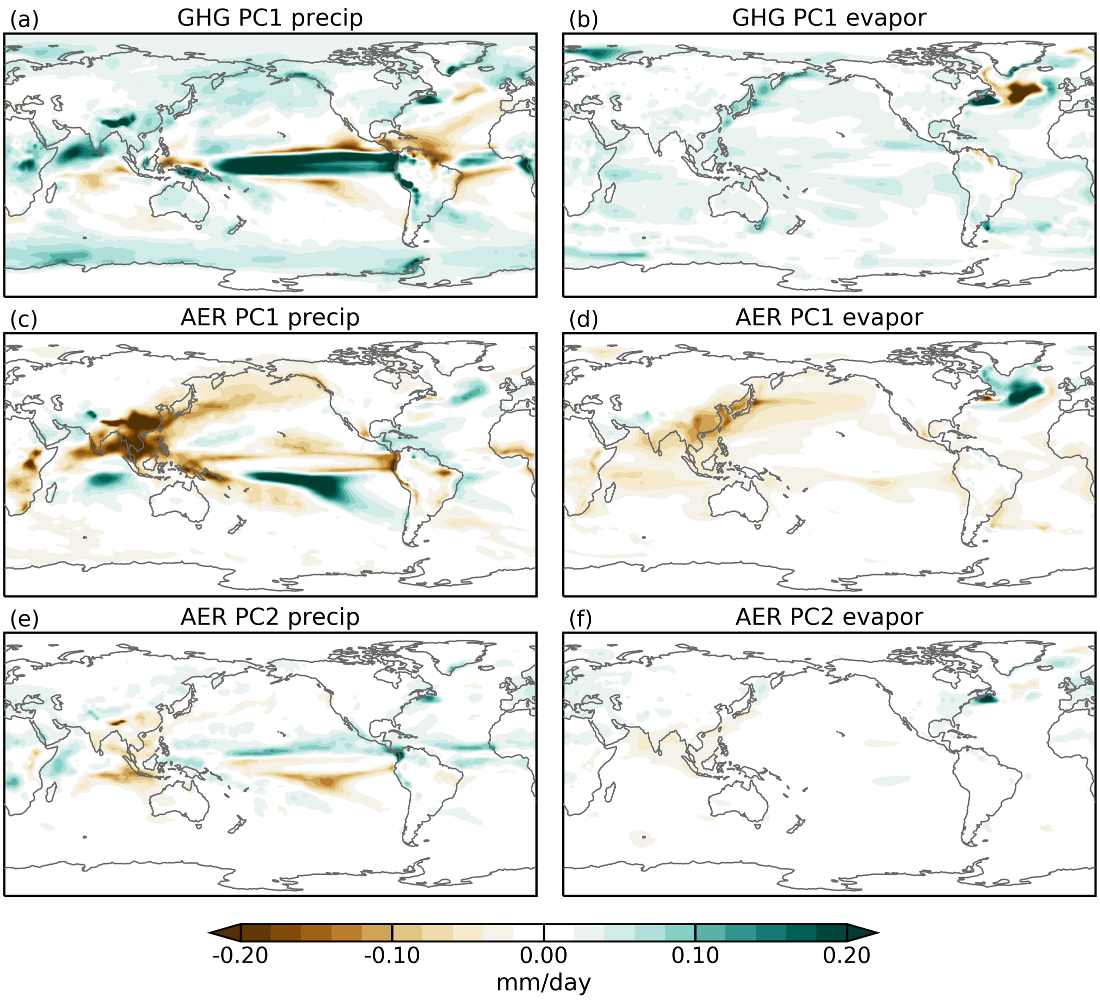

Figure S1. Precipitation (left) and evaporation (right) regressions onto GHG PC1 (top), AER PC1 (middle) and AER PC2 (bottom). Units: mm/day/std.

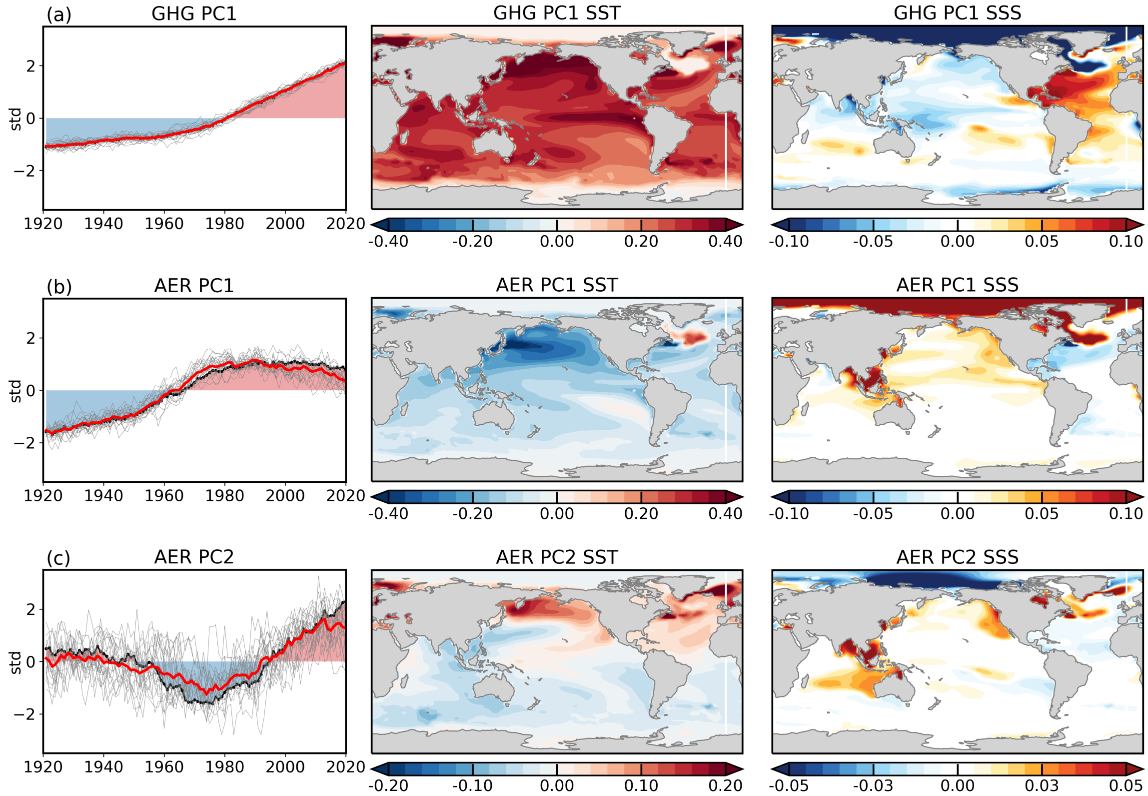

Figure S2. Results of LFCA applied to each of the individual ensemble members. (left) PC time series. Grey lines are individual members; black lines and color filling are the average of all members; red lines are the LFCA results applied to the ensemble-mean response as in Fig. 2. (middle) SST and (right) SSS patterns are averaged over all individual members' PC patterns.

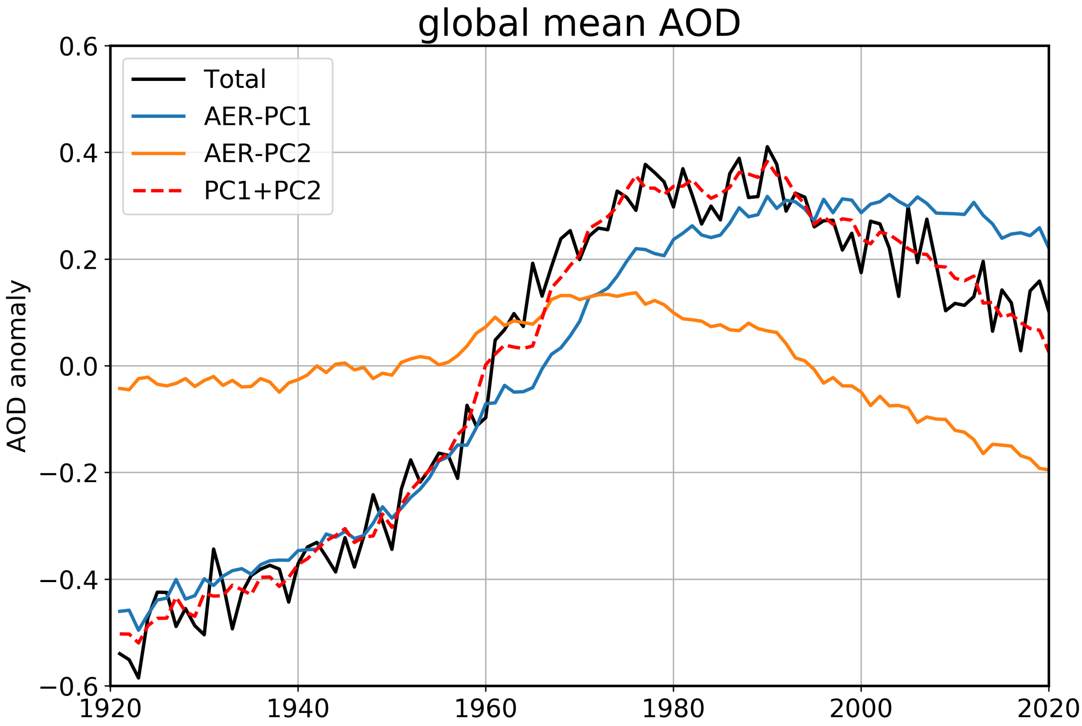

Figure S3. Global-mean AOD anomalies (relative to 1921-2020 climatology) from AER simulations (black) and PC reconstructions (blue and orange). Red dashed line denotes the sum of PC1 and PC2 associated AOD anomalies.

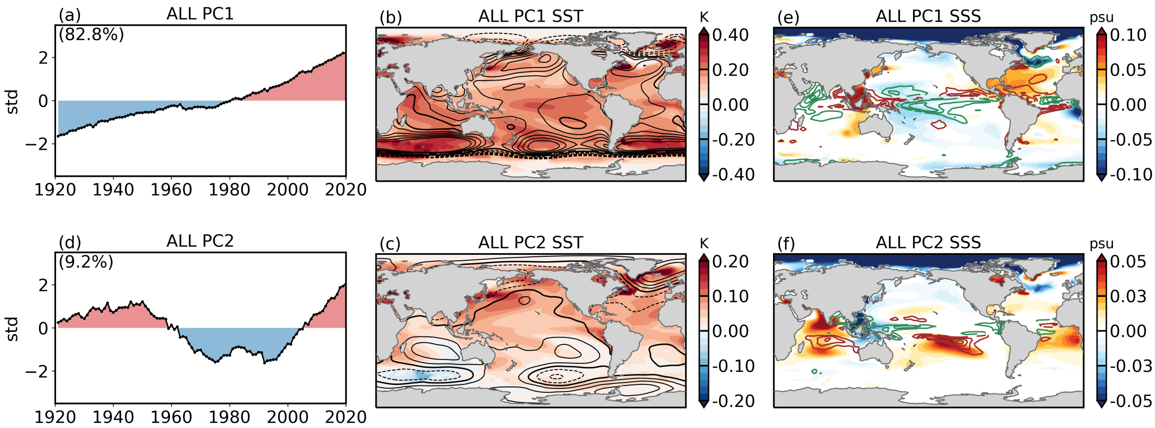

Figure S4. Same with Fig. 2 except for the two leading modes obtained from CESM1 ALL ensemble-mean responses.

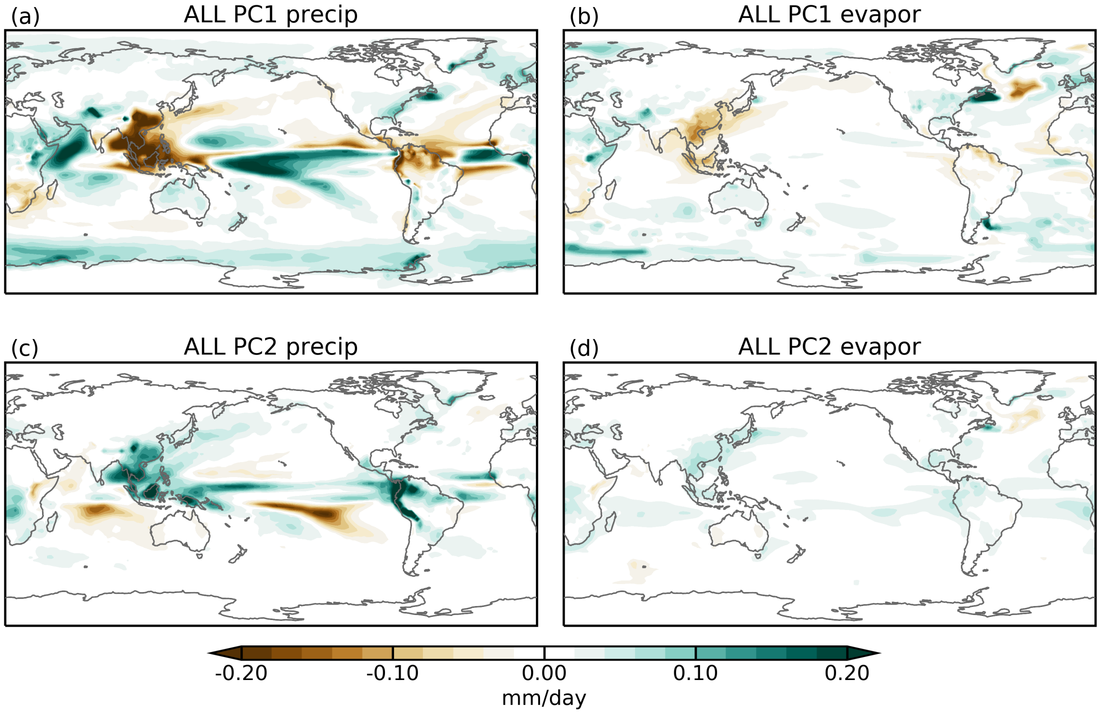

Figure S5. Regressions of (left) precipitation and (right) evaporation onto ALL PC1 and PC2.